

# Focusing the Latent Heat Release in 3D Phase Field Simulations of Dendritic Crystal Growth

Pavel Strachota<sup>a,\*</sup>, Aleš Wodecki<sup>a</sup>, Michal Beneš<sup>a</sup>

<sup>a</sup>*Department of Mathematics, Faculty of Nuclear Sciences and Physical Engineering, Czech Technical University in Prague. Trojanova 13, 120 00 Praha 2, Czech Republic*

## Abstract

We investigate a family of phase field models for simulating dendritic growth of a pure supercooled substance. Our aim is to remove limitations inherent to some existing models both in terms of the applicability to physically realistic situations and the feasibility of mathematical and numerical analysis. The central object of interest is the reaction term in the Allen-Cahn equation, which is responsible for spatial distribution of latent heat release during solidification. Several existing forms of the reaction term are analyzed and new variants are proposed, with consistent asymptotic behavior as the interface thickness tends to zero. The resulting models are tested in a number of numerical simulations focusing on mesh-dependence, model parameter settings, and the applicability to solidification under very large supercooling.

**Keywords:** Allen-Cahn equation, dendritic crystal growth, diffuse phase interface, phase field, rapid solidification, reaction term

## 1. Introduction

Phase field modeling [1, 2] has been a popular and universal tool for solving moving boundary problems in materials science for more than three decades now. The theoretical foundations laid out by Allen and Cahn [3] were later utilized by Caginalp [4, 5] to show the relation between the diffuse interface and sharp interface models of phase transition phenomena. Anisotropic dendritic crystal growth in pure supercooled melts [6, 7, 8, 9] and binary alloys [10] was first simulated numerically in 2D. Later, single-crystal 3D simulations were performed by Karma and his collaborators [11] and the used models evolved further to predict quantitative properties of crystal growth [12, 13, 14, 15]. More recent studies by many authors have been focusing e.g on multicomponent alloys [16], interaction with fluid flow [17], grain growth [18, 19, 20], polycrystalline solidification [21], and efficient numerical methods for very large scale parallel simulations [22, 23, 24]. There have also been many applications of the phase field approach to problems beyond the scope of materials science such as [25, 26, 27, 28].

In this paper, we investigate a family of phase field models for simulating dendritic growth of a pure supercooled substance designed in our previous work [29] and related to [7]. These models were used in qualitative computational studies in both 2D [29, 30, 31] and 3D [32] and efficient parallel numerical solvers were implemented by means of the finite volume method [33]. Extensions to polycrystalline solidification were

also implemented [34, 35]. We review the behavior of several existing models with different reaction terms in the Allen-Cahn [3] equation. Depending on the particular variant of the model, limitations exist in terms of the applicability to physically realistic situations, in terms of the possible mathematical and numerical analysis, or both. We see the reaction term as means for controlling the spatial distribution of latent heat release during solidification. Its form can be adjusted while the asymptotic behavior of the model remains valid [4, 36]. We take advantage of this flexibility and propose a new variant of the reaction term. The resulting model is compatible with the numerical analysis performed in our paper [37] for the finite volume method (as long as anisotropy is not considered) and it also achieves a very good quantitative agreement with experiments in the numerically difficult case of rapid solidification. In a number of simulations, we compare the behavior of the discussed models.

## 2. Analysis of the existing models

The works [4, 5] and [29] view the phase field formulation as an approximation of some corresponding sharp interface description. For our discussion, the reference sharp interface model is the isotropic Stefan problem with surface tension [38]. For the sake of simplicity and intuitive interpretation, we proceed from an isotropic setting despite the fact that our simulations mainly use anisotropy in agreement with physical reality. Note however that the anisotropic case introduced later in Section 4 can also be treated by a similar procedure [39, 40].

### 2.1. Stefan problem with surface tension

Consider a domain  $\Omega \subset \mathbb{R}^3$  and the time interval  $\mathcal{J} = (0, T)$ . At each time  $t$ ,  $\Omega$  is divided into the solid subdomain  $\Omega_s(t)$  and

\*Corresponding author. Phone: +420 224 358 563

Email addresses: pavel.strachota@fjfi.cvut.cz (Pavel Strachota), ales.wodecki@fjfi.cvut.cz (Aleš Wodecki), michal.benes@fjfi.cvut.cz (Michal Beneš)

Table 1: Physical quantities in the Stefan problem with surface tension

Quantity	SI Units	Description
$u$	K	temperature
$\rho$	$\text{kg} \cdot \text{m}^{-3}$	density
$c$	$\text{J} \cdot \text{kg}^{-1} \text{K}^{-1}$	specific heat capacity
$\lambda$	$\text{W} \cdot \text{m}^{-1} \cdot \text{K}^{-1}$	heat conductivity
$L$	$\text{J} \cdot \text{m}^{-3}$	latent heat of fusion per unit vol.
$u^*$	K	melting point
$\sigma$	$\text{J} \cdot \text{m}^{-2}$	surface tension
$\Delta s$	$\text{J} \cdot \text{m}^{-3} \cdot \text{K}$	entropy difference per unit volume
$\mu$	$\text{m} \cdot \text{s}^{-1} \cdot \text{K}^{-1}$	interface mobility (see [10, 6])
$\alpha$	$\text{m}^{-1} \cdot \text{s}$	coef. of attachment kinetics $\alpha = \frac{\Delta s}{\mu \sigma}$
$\beta$	$\text{m}^{-1} \cdot \text{K}^{-1}$	$\beta = \frac{\Delta s}{\sigma}$

Table 2: Dimensionless quantities

Dim-less qty	Definition	Description
$\tilde{u}$	$(u - u^*) / \Delta u_{\text{ini}} + 1$	temperature
$\tilde{L}$	$L / (\rho c \Delta u_{\text{ini}})$	latent heat
$L_0$	user-defined	length scale
$t_0$	$(\rho c / \lambda) L_0^2$	time scale
$\tilde{\alpha}$	$(\lambda / (\rho c)) \alpha$	attachment kinetics coef.
$\tilde{\beta}$	$\beta L_0 \Delta u_{\text{ini}}$	
$\tilde{\mathbf{x}}$	$\mathbf{x} / L_0$	dimensionless position
$\tilde{t}$	$t / t_0$	dimensionless time

also obtain the dimensionless normal velocity of the interface

$$\tilde{v}_\Gamma(\tilde{t}) = \frac{t_0}{L_0} v(t)$$

and the dimensionless interface mean curvature

$$\tilde{\kappa} = L_0 \kappa.$$

The Gibbs-Thomson relation (5) transformed into dimensionless quantities therefore remains in the same form

$$\tilde{\beta}(\tilde{u} - \tilde{u}^*) = -\tilde{\kappa}_\Gamma - \tilde{\alpha} \tilde{v}_\Gamma. \quad (7)$$

From this point on, we will only deal with dimensionless quantities unless stated otherwise. For better readability, the tildes over the respective dimensionless quantities will be omitted.

### 2.3. General form of the phase field equations

Let  $p : \mathcal{J} \times \Omega \mapsto [0, 1]$  be the phase field equal to 0 in the liquid phase and 1 in the solid phase, with a smooth transition in between. The evolution of the phase interface  $\Gamma$  can be determined implicitly by the relation

$$\Gamma(t) = \left\{ \mathbf{x} \in \Omega \mid p(t, \mathbf{x}) = \frac{1}{2} \right\}. \quad (8)$$

Following [29, 4], the governing system of equations in dimensionless form corresponding to the problem (1)–(6) reads

$$\frac{\partial u}{\partial t} = \Delta u + L \frac{\partial p}{\partial t} \quad \text{in } \mathcal{J} \times \Omega, \quad (9)$$

$$\alpha \xi^2 \frac{\partial p}{\partial t} = \xi^2 \Delta p + f(u, p, \nabla p; \xi) \quad \text{in } \mathcal{J} \times \Omega, \quad (10)$$

$$u|_{t=0} = 0, \quad p|_{t=0} = p_{\text{ini}} \quad \text{in } \Omega, \quad (11)$$

coupled with either Dirichlet or homogeneous Neumann boundary conditions chosen independently for  $u$  and  $p$ , i.e.

$$u|_{\partial\Omega} = u_{\partial\Omega} \text{ or } \nabla u \cdot \mathbf{n} = 0 \text{ on } \mathcal{J} \times \partial\Omega \quad (12)$$

and

$$p|_{\partial\Omega} = p_{\partial\Omega} \text{ or } \nabla p \cdot \mathbf{n} = 0 \text{ on } \mathcal{J} \times \partial\Omega. \quad (13)$$

The particular form of the reaction term  $f(u, p, \nabla p; \xi)$  distinguishes between the individual models and will be discussed later in Section 2.5. The role of the small scalar parameter  $\xi > 0$  is shown below.

the liquid subdomain  $\Omega_l(t) = \Omega \setminus \Omega_s(t)$  by the phase interface  $\Gamma(t)$ . Further on, let us introduce the notation in Table 1.

The system of governing equations reads

$$\rho c \frac{\partial u}{\partial t} = \nabla(\lambda \nabla u) \quad \text{in } \mathcal{J} \times \Omega_s(t) \quad (1)$$

and  $\mathcal{J} \times \Omega_l(t)$ ,

$$b_c(u)|_{\partial\Omega} = 0 \quad \text{on } \mathcal{J} \times \partial\Omega, \quad (2)$$

$$u|_{t=0} = u^* - \Delta u_{\text{ini}} \quad \text{in } \Omega, \quad (3)$$

$$\lambda \frac{\partial u}{\partial n_\Gamma} \Big|_s - \lambda \frac{\partial u}{\partial n_\Gamma} \Big|_l = L v_\Gamma \quad \text{on } \Gamma(t), \quad (4)$$

$$\beta(u - u^*) = -\kappa_\Gamma - \alpha v_\Gamma \quad \text{on } \Gamma(t), \quad (5)$$

$$\Omega_s(0) = \Omega_{s,\text{ini}}. \quad (6)$$

The problem consists of the heat equation (1) valid within both subdomains, the Stefan condition (4) expressing the discontinuity of the heat flux across the interface  $\Gamma(t)$  and the Gibbs-Thomson relation (5) describing the normal velocity of the interface  $v_\Gamma$  as a function of both the supercooling and the interface mean curvature  $\kappa_\Gamma$ . The conditions (3) and (6) prescribe the uniform initial supercooling  $\Delta u_{\text{ini}} > 0$  and the spatial distribution of the solid and liquid phase. The boundary condition (2) for temperature can be of Dirichlet type, prescribing the temperature  $u_{\partial\Omega}$  on  $\partial\Omega$  by

$$b_c(u) = u - u_{\partial\Omega},$$

or of Neumann type, specifying the heat flux  $\mathbf{g}$  through  $\partial\Omega$  by

$$b_c(u) = (\lambda \nabla u - \mathbf{g}) \cdot \mathbf{n}.$$

### 2.2. Dimensionless formulation

We intend to introduce the phase field model in the dimensionless form, which can be achieved by defining the quantities (recognized by tilde over the respective symbols) according to Table 2. These relations imply that the initial supercooling  $\Delta u_{\text{ini}}$  scales the value of  $\tilde{\beta}$ , whereas the dimensionless melting point is always  $\tilde{u}^* = 1$ . Similarly, the dimensionless initial temperature satisfies  $\tilde{u}|_{t=0} = 0$  independently of  $\Delta u_{\text{ini}}$ . Furthermore, we

#### 2.4. Results of the matched asymptotic analysis

The correspondence between the phase field model (9)–(13) and the Stefan problem (1)–(6) is investigated by means of matched asymptotic analysis for  $\xi \rightarrow 0$ , explained in detail in [4] and performed for the above model in [36]. Here we only cherry-pick the important results that will be of utility for the subsequent scrutiny and development.

Let us consider the reaction term in the form (corresponding to the expansion of  $f$  into the powers of  $\xi$  up to the first order)

$$f(u, p, \nabla p; \xi) = f_0(p) + \xi f_1(u, p, \nabla p; \xi)$$

where

$$f_0(p) = 2p(1-p) \left( p - \frac{1}{2} \right).$$

The choice of the term  $f_0(p)$  represents the derivative of the double-well potential [4]. For  $\xi$  sufficiently small, it ensures that  $f$  as a function of  $p$  has roots in the vicinity of 0, 1, and  $\frac{1}{2}$ , and that  $p$  close to zero is attracted to zero, whereas  $p$  close to one is attracted to one, giving rise to a thin interface layer in between.

The inner asymptotic expansion indicates the profile of the phase field  $p$  across the interface  $\Gamma(t)$  given by (8), matching the values obtained from the outer expansion. In simple terms, for  $\mathbf{x}_0 \in \Gamma(t)$ , we introduce a coordinate  $z$  and a function  $\bar{p}$  such that for a given time  $t \in \mathcal{J}$ , we have

$$\bar{p}(z) = p(t, \mathbf{x}_0 + \xi z \mathbf{n}_\Gamma),$$

$\mathbf{n}_\Gamma$  being the normal vector to  $\Gamma$  at  $\mathbf{x}_0$  pointing in the direction outside of the solid subdomain. Then the function  $\bar{p}$  satisfies

$$\bar{p}(z) = \bar{p}_{\text{asy}}(z) + o(\xi) \quad \text{where} \quad \bar{p}_{\text{asy}}(z) = \frac{1}{2} \left[ 1 - \tanh\left(\frac{z}{2}\right) \right]. \quad (14)$$

The graph of  $\bar{p}_{\text{asy}}$  is depicted in Figure 1. This graph indicates that the diffuse interface (where  $\bar{p}$  is neither almost zero or almost one) effectively spans a range  $z \in (-5, 5)$ , yielding a thickness of approximately  $10\xi$  in the original coordinates. This is important for choosing the mesh resolution in numerical simulations. Our simulations (see Section 5) confirm that it is usually enough to have mesh element size equal to  $\xi$ , which results in roughly 10 mesh elements available to approximate  $p$  across the interface.

The other important result is the asymptotic recovery of the Gibbs-Thomson relation as  $\xi \rightarrow 0$ . Depending on the form of  $f$ , this relation has the form [36]

$$\frac{\mathcal{I}_1}{\mathcal{I}_2} = -\kappa_\Gamma - \alpha v_\Gamma \quad (15)$$

where

$$\mathcal{I}_1 = \int_{-\infty}^{+\infty} f_1(\bar{u}, \bar{p}, \frac{d\bar{p}}{dz}) \frac{d\bar{p}}{dz} dz$$

and the form of  $f_0$  yields

$$\mathcal{I}_2 = \frac{1}{6}.$$

In various forms of the term  $f_1$ , it is possible to tweak the suitable constants so that (15) becomes the Gibbs-Thomson relation of the Stefan problem (7).

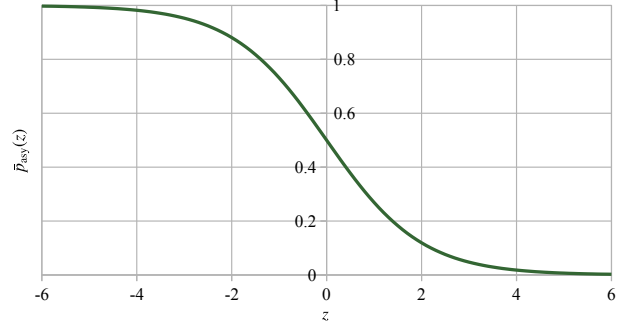


Figure 1: The asymptotic profile of the phase field (the value of  $\bar{p}_{\text{asy}}(z)$ ) across the diffuse interface given by (14).

#### 2.5. Some known variants of the reaction term

We review the formulation and properties of some existing reaction terms, which motivates the design of the improved reaction term variants further in Section 3.

##### 2.5.1. The linear model

Let us start with the simple version of the reaction term used in [4], namely

$$f_1(u) = b\beta(u^* - u), \quad (16)$$

$\Downarrow$

$$f(u, p; \xi) = 2p(1-p) \left( p - \frac{1}{2} \right) + \xi b\beta(u^* - u).$$

The recovery of the Gibbs-Thomson relation (7) requires that  $b = \mathcal{I}_2$ . This model has two major drawbacks that demonstrate themselves for practical simulations with  $\xi$  fixed. First, it is immediately apparent that thanks to the form of  $f_1$ ,  $f$  has nonzero values even for  $p = 0$  and  $p = 1$ , so that latent heat is released in the whole domain (not only at the interface) until an equilibrium is achieved with values of  $p$  shifted away from 0 and 1. Second, the minimum of  $f_0$  for  $p \in [0, 1]$  has the value  $-\frac{\sqrt{3}}{18}$ . As the initial dimensionless supercooling  $u^* - u|_{t=0}$  is always equal to 1, the condition

$$\xi b\beta = \frac{1}{6}\xi\beta < \frac{\sqrt{3}}{18} \iff \xi\beta < \frac{\sqrt{3}}{3} \quad (17)$$

is necessary for  $f$  to maintain its three roots so that the interface can develop its characteristic profile. For any realistic value of  $\beta$ , this requires  $\xi$  to be chosen very small and the mesh resolution extremely fine (see Section 2.4 above), which is not possible even on contemporary computers, especially for 3D simulations.

##### 2.5.2. The Kobayashi model

In [7], the author proposes the reaction term in the form

$$f_1(u, p; \xi) = 2p(1-p) \frac{\alpha}{\pi\xi} \arctan(\gamma(u^* - u)), \quad (18)$$

$\Downarrow$

$$f(u, p; \xi) = 2p(1-p) \left( p - \frac{1}{2} + \frac{\alpha}{\pi} \arctan(\gamma(u^* - u)) \right).$$

For  $\alpha \in (0, 1)$ , this model ensures that for any  $\gamma$ ,  $f$  retains three roots:  $p_0 = 0$ ,  $p_1 = 1$ , and the third one  $p_2 \in (0, 1)$ . This means that latent heat exchange is focused on the diffuse interface only. No latent heat exchange occurs in pure solid and pure liquid. However, the use of arctangent yields almost linear dependence of solidification speed on supercooling (as given by (7)) only for small values of  $\gamma = \xi\beta$ . With increasing values of supercooling, this model remains well-posed, but the asymptotic recovery of the Gibbs-Thomson relation is lost.

### 2.5.3. The gradient model (a.k.a. GradP model)

In [29, 36], the reaction term is proposed in the form

$$f_1(u, p, \nabla p; \xi) = \xi b \beta |\nabla p| (u^* - u), \quad (19)$$

$\Downarrow$

$$f(u, p, \nabla p; \xi) = 2p(1-p) \left( p - \frac{1}{2} \right) + \xi^2 b \beta |\nabla p| (u^* - u)$$

and to recover the Gibbs-Thomson relation (7), it is calculated that  $b = 1$ . This model has notable computational advantages. It is obvious that  $|\nabla p| = 0$  when  $p$  is constant, and therefore the term  $f$  continues to have three roots almost exactly at 0, 1,  $\frac{1}{2}$  in the bulk solid and liquid. The latent heat release is focused at the interface where the gradient is nonzero. Several computational studies have been performed using this model, both in 2D [30, 41, 29, 42] and in 3D [32, 33, 34]. However, for a very large supercooling, this model seems to be failing as well (see Section 5.5). The gradient term also introduces difficulties into the numerical analysis of finite difference [30] and finite volume [32] schemes.

## 3. Designing alternative reaction terms

In the following, we try to design a novel alternative to the gradient reaction term in order to:

1. Simplify the numerical analysis of the resulting phase field model. By constructing a local reaction term (depending on  $p$  and  $u$  only) and possibly enforcing its boundedness by an appropriate constant, the finite volume and finite difference schemes (see e.g. [32, 39]) get simpler and the analysis of convergence of the numerical solution to the unique solution of the original problem becomes possible, as shown in our work [37].
2. Make the model applicable to simulations with very large values of supercooling.

### 3.1. The $\Sigma P1$ -P model

The forms of the reaction term  $f_1$  differ in the way how the thermodynamic driving force (and the latent heat release) is distributed or focused in the spatial domain  $\Omega$ . As the gradient model (19) is known to work well in a relatively wide range of supercooling values and other parameter settings, we try to construct a local term that would provide a similar distribution of latent heat release.

A natural idea is to replace the gradient of the solution  $p$  which for a given  $t \in \mathcal{J}$  and  $\mathbf{x}_0 \in \Gamma(t)$  satisfies

$$\nabla p(\mathbf{x}_0) = -\frac{\partial p}{\partial \mathbf{n}_\Gamma}(\mathbf{x}_0) = -\frac{1}{\xi} \frac{d\bar{p}}{dz}(0)$$

by the derivative of the asymptotic profile  $\bar{p}_{\text{asy}}$  (14) across the interface. Directly from the matched asymptotic analysis (see [36] for details) or by differentiation of (14), it follows that  $\bar{p}_{\text{asy}}$  satisfies the differential equation

$$\frac{d\bar{p}_{\text{asy}}}{dz} = -2\bar{p}_{\text{asy}}(1 - \bar{p}_{\text{asy}}).$$

By replacing  $|\nabla p|$  by  $\frac{1}{\xi} 2p(1-p)$  (which is nonnegative for all  $p \in [0, 1]$ ) in (19), we arrive at the reaction term in the form

$$f_1(u, p) = b\beta 2p(1-p)(u^* - u), \quad (20)$$

$\Downarrow$

$$f(u, p; \xi) = 2p(1-p) \left( p - \frac{1}{2} + \xi b \beta \frac{1}{2} (u^* - u) \right).$$

In principle, an equivalent formula has already been mentioned in [7] as a precursor of the Kobayashi model (18).

Evaluating the asymptotic Gibbs-Thomson relation (15), we first find that

$$\mathcal{I}_1 = b\beta(u^* - u) \int_0^1 p(1-p) dp = b\beta \mathcal{I}_2(u^* - u),$$

which implies the recovery of the original Gibbs-Thomson relation (7) for  $b = 1$ , as in the gradient model (19).

The reaction term  $f$  given by (20) has the roots  $p_0 = 0$ ,  $p_1 = 1$  just like in the Kobayashi model (18). However, the existence of the third root  $p_2 \in (0, 1)$  and hence the proper formation of the diffuse interface is bound by the condition

$$\xi\beta < 1$$

which is similar to (17) and only satisfied for small values of supercooling. To relax this condition, we propose a modified version

$$f_1(u, p) = b\beta \Sigma(p; \varepsilon_0, \varepsilon_1) p(1-p)(u^* - u), \quad (21)$$

$\Downarrow$

$$f(u, p; \xi) = 2p(1-p) \left( p - \frac{1}{2} + \xi b \beta \frac{1}{2} \Sigma(p; \varepsilon_0, \varepsilon_1) (u^* - u) \right),$$

where  $\Sigma(p; \varepsilon_0, \varepsilon_1)$  is a differentiable sigmoid function (a limiter) in the form

$$\Sigma(p; \varepsilon_0, \varepsilon_1) = \begin{cases} 0 & p \leq \varepsilon_0, \\ 1 & p \geq \varepsilon_1, \\ \frac{3(p-\varepsilon_0)^2}{(\varepsilon_1-\varepsilon_0)^2} - \frac{2(p-\varepsilon_0)^3}{(\varepsilon_1-\varepsilon_0)^3} & p \in (\varepsilon_0, \varepsilon_1). \end{cases} \quad (22)$$

By multiplying the thermodynamic force term by  $\Sigma$  which is (close to) zero for  $p \approx 0$ , the existence of the third root  $p_2 \in (0, 1)$  and thus the expected behavior of the model is ensured

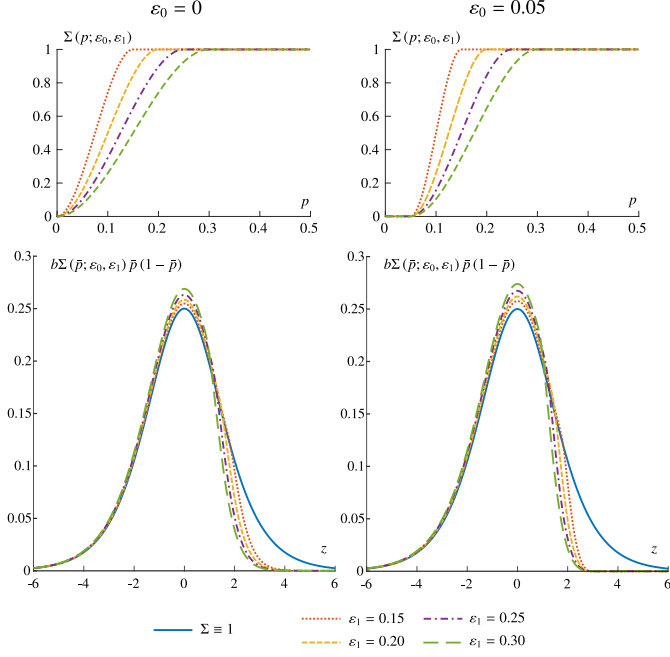


Figure 2: Plots of  $\Sigma(p; \varepsilon_0, \varepsilon_1)$  for different values of  $\varepsilon_0, \varepsilon_1$  (top row) and of the term  $b\Sigma(\bar{p}(z); \varepsilon_0, \varepsilon_1) \bar{p}(z)(1 - \bar{p}(z))$  which is proportional to the latent heat release rate across the asymptotic profile of the diffuse interface (14) (bottom row). The value of  $b$  depends on  $\varepsilon_0, \varepsilon_1$  as given by (23).

independently of  $\beta$ , i.e. for virtually any value of supercooling. The choice of  $\varepsilon_0, \varepsilon_1$  that works properly in the numerical algorithm will be discussed further in Section 5.3.

In order to asymptotically satisfy (7), we calculate

$$\mathcal{I}_1 = b\beta(u^* - u) \int_0^1 \Sigma(p; \varepsilon_0, \varepsilon_1) p(1 - p) dp$$

After plugging the result into (15), we find that  $b$  needs to be chosen as

$$b = \frac{1}{6} \left( \frac{\varepsilon_0^3}{15} + \frac{\varepsilon_0^2 \varepsilon_1}{10} - \frac{3\varepsilon_0^2}{20} - \frac{\varepsilon_0 \varepsilon_1}{5} + \frac{\varepsilon_0 \varepsilon_1^2}{10} - \frac{3\varepsilon_1^2}{20} + \frac{\varepsilon_1^3}{15} + \frac{1}{6} \right). \quad (23)$$

The shape of the  $\Sigma$  limiter (22) and the corresponding profiles of latent heat release across the diffuse interface are plotted in Figure 2.

### 3.2. The $\Sigma$ GradP model

The gradient model (19) can also be modified by incorporating  $\Sigma$  and obtaining the reaction term in the form

$$\begin{aligned} f_1(u, p, \nabla p; \xi) &= \xi b \Sigma(p; \varepsilon_0, \varepsilon_1) |\nabla p| (u^* - u), \\ \Downarrow \\ f(u, p, \nabla p; \xi) &= 2p(1 - p) \left( p - \frac{1}{2} \right) + \xi^2 b \Sigma(p; \varepsilon_0, \varepsilon_1) |\nabla p| (u^* - u). \end{aligned} \quad (24)$$

This modification may contribute to the stability of the phase interface when large supercooling is used and the gradient model ceases to work correctly. Some results calculated using the reaction term (24) are shown in Section 5.5.

### 3.3. Modeling irregular growth

To obtain more realistic simulation results, random noise that modifies the reaction term can be used [7]. Loosely inspired e.g. by [43], we propose to use a time independent continuous noise field

$$\hat{u} : \Omega \rightarrow \left[ -\frac{1}{2}, \frac{1}{2} \right] \quad (25)$$

satisfying

$$\int_{\Omega} \hat{u}(x) dx = 0$$

and introduce thermal fluctuations to the reaction term by replacing  $f(u, p, \nabla p; \xi)$  by  $f(u + \delta \hat{u}, p, \nabla p; \xi)$  in (10). The perturbation amplitude is controlled by the parameter  $\delta \geq 0$ .

## 4. The anisotropic phase field model

To incorporate anisotropy, we follow the approach of Finsler geometry as introduced by [44] and later used in a number of our previous works, e.g. [41, 30, 40, 45, 33, 32, 46].

The anisotropic phase field model arises by replacing equation (10) by

$$\alpha \xi^2 \frac{\partial p}{\partial t} = \xi^2 \nabla \cdot T^0(\nabla p) + f(u, p, \nabla p; \xi) \quad \text{in } \mathcal{J} \times \Omega \quad (26)$$

and the boundary condition (13) by

$$T^0(\nabla p) \cdot \mathbf{n} = 0 \quad \text{on } \mathcal{J} \times \partial\Omega. \quad (27)$$

The anisotropic operator  $T^0$  (see [44, 41, 30]) is derived from the convex dual Finsler metric  $\phi^0(\boldsymbol{\eta}^*)$ ,  $\boldsymbol{\eta}^* \in \mathbb{R}^3$  as

$$T^0(\boldsymbol{\eta}^*) = \phi^0(\boldsymbol{\eta}^*) \phi_{\boldsymbol{\eta}}^0(\boldsymbol{\eta}^*) \quad \text{where } \phi_{\boldsymbol{\eta}}^0 = \left( \partial_{\eta_1^*} \phi^0, \partial_{\eta_2^*} \phi^0, \partial_{\eta_3^*} \phi^0 \right)^T. \quad (28)$$

The choice  $\boldsymbol{\eta}^* = \nabla p$  in (26) and (27) ensures that

$$\mathbf{n} = -\frac{\boldsymbol{\eta}^*}{|\boldsymbol{\eta}^*|} \quad (29)$$

is the outer normal to  $\Gamma$  for  $\mathbf{x} \in \Gamma$ .

If the function  $\psi : \mathbb{R}^3 \rightarrow (0, +\infty)$  represents the anisotropic surface energy depending on the normal  $\mathbf{n}$ ,  $\phi^0$  assumes the form [47, 48]

$$\phi^0(\boldsymbol{\eta}^*) = |\boldsymbol{\eta}^*| \psi(\mathbf{n}). \quad (30)$$

For example, the formula for 4-fold anisotropy aligned with the specimen coordinate system reads [49]

$$\psi(\mathbf{n}) = 1 + A_1 \left[ n_1^4 + n_2^4 + n_3^4 - 6(n_1^2 n_2^2 + n_2^2 n_3^2 + n_3^2 n_1^2) \right] \quad (31)$$

where the coefficient  $A_1 \ll 1$  specifies the anisotropy strength.

### 4.1. Reaction terms in the anisotropic model

The reaction term  $f$  in (26) can assume any of the forms (16), (18), (19), (21), (24). In addition, the gradient model (19) and the  $\Sigma$ GradP model (24) can be further modified by replacing  $|\nabla p|$  by the anisotropic norm  $\phi^0(\nabla p)$ . In practice, this modification slightly increases the solidification rate where the outer normal to the solid-liquid interface points in the preferred directions of dendrite growth. The resulting models will be referred to as  $\phi^0$ GradP and  $\Sigma\phi^0$ GradP, respectively. Noise can be added to (26) exactly as described in Section 3.3.

## 5. Computational studies

The primary purpose of the computational studies shown below is to understand the behavior of the  $\Sigma$ P1-P model (21) in comparison to the original GradP model (19) and its anisotropic variant (the  $\phi^0$ GradP model). The phase field model with anisotropy given by equations (9), (26), (11), (12), and (13) is used.

All simulations were performed using our efficient hybrid OpenMP/MPI parallel implementation [33] of the numerical solver based on multipoint flux approximation finite volume scheme on a uniform rectangular mesh [32] and 4th order Runge-Kutta-Merson integrator with adaptive stepping in time [50]. Note that keeping the random noise field (25) constant in time guarantees that the time step adjustment algorithm is not affected.

### 5.1. Initial & boundary conditions, parameter settings

The domain  $\Omega$  is a cube in the form  $\Omega = (0, \ell)^3$  discretized by a uniform mesh of  $N \times N \times N$  cells. The values of  $\ell$  and  $N$  together with the anisotropy specification vary and are reported separately for each of the studies. Zero Neumann boundary conditions are chosen for both  $u$  and  $p$  which allows to initiate the solidification at a spherical nucleation site  $\Omega_s(0)$  located either in the center or in the corner of the domain  $\Omega$ . In the latter case,  $\Omega$  represents one octant of a larger domain where centrally and axially symmetric solidification takes place. The initial condition (11) for the phase field is given by

$$p_{\text{ini}}(\mathbf{x}) = \begin{cases} 1 & \mathbf{x} \in \Omega_s(0), \\ 0 & \mathbf{x} \in \Omega_l(0) = \Omega \setminus \Omega_s(0). \end{cases}$$

Except in Section 5.5, a reference set of parameters comparable to the choices in [29, 7] is specified as  $\alpha = 3$ ,  $\beta = 300$ ,  $\xi = 0.011$ ,  $L = 2$ . Noise is not used unless a positive value of  $\delta$  is explicitly given.

### 5.2. Latent heat release profiles at the diffuse interface

In order to evaluate the difference between the GradP and the  $\Sigma$ P1-P models in terms of latent heat release focusing, we extracted the profiles of  $p$  across the diffuse phase interface from numerical simulations and compared them to the asymptotic profile  $p_{\text{asy}}$ . The computations were performed in a domain of size  $\ell = 4$  with mesh resolutions  $N \in \{100, 200, 800\}$  and  $\xi = 0.011$ . We verified that the diffuse interface forms shortly after the start of the simulation and the use of anisotropy, the location of readout of the values of  $p$  along the interface and the choice of the model all have a negligible effect on its shape. Figure 3 demonstrates the subtle difference between  $p$  and  $p_{\text{asy}}$  on different meshes. In addition, the quantities  $|\nabla p|$ ,  $\frac{1}{\xi}2p(1-p)$  occurring in the GradP and the  $\Sigma$ P1-P models, respectively, are plotted.

### 5.3. Effect of $\varepsilon_0, \varepsilon_1$ in the $\Sigma$ P1-P model

To investigate the role of  $\varepsilon_0, \varepsilon_1$  in the  $\Sigma$ P1-P model, simulations with

$$\varepsilon_0 \in \{0, 0.05\}, \quad \varepsilon_1 \in \{0.15, 0.20, 0.25, 0.30\}$$

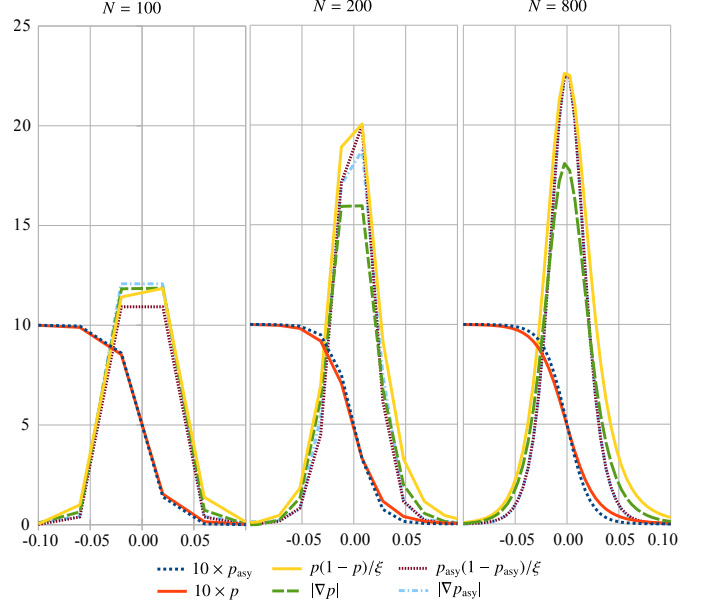


Figure 3: The computed profiles of  $p$  across the diffuse phase interface compared to the asymptotic profile  $p_{\text{asy}}$  on meshes with different resolutions. The horizontal axis represents the  $\xi z$  coordinate, i.e. the signed distance from the phase interface. Based on both  $p$  and  $p_{\text{asy}}$ , the key quantities determining the latent heat release profile across the interface are evaluated for the GradP and the  $\Sigma$ P1-P models. The gradients are calculated numerically by 4th order central differences also used in the numerical scheme (see Section 5), which explains why  $|\nabla p_{\text{asy}}|$  and  $p_{\text{asy}}(1 - p_{\text{asy}})/\xi$  do not coincide.

were performed, which corresponds to the solidification focusing profiles shown in Figure 2. An even lower value  $\varepsilon_1 = 0.1$  was not enough for the diffuse interface to form correctly. The results were obtained with  $\ell = 6$ ,  $N = 400$ , 4-fold anisotropy given by (31) with  $A_1 = 0.02$ . The nucleation site with radius 0.05 was located in the corner of  $\Omega$  at  $\mathbf{x} = \mathbf{0}$  and the snapshots at time  $t = 0.26$  were compared. As noise was not used, it is possible to demonstrate only part of the whole crystal, the rest being given by symmetry. By this approach, up to eight shapes can be compared in different sectors of space viewed in the direction of the  $z$  axis, as shown in Figures 4 and 5.

First, Figure 4 compares the crystal shapes with  $b$  in (21) fixed to 1 instead of being given by (23). The model therefore deviates from the Gibbs-Thomson condition (7) and significant differences in results depending on the values of  $\varepsilon_0, \varepsilon_1$  are obtained, as expected. In Figure 5, the value of  $b$  is given by (23), but nonetheless the results stay very similar to those in Figure 4. This observation testifies that the evolution of the complex dendritic structure is very sensitive to changing the focusing of latent heat release, despite the fact that the asymptotic behavior for  $\xi \rightarrow 0$  should be the same regardless of  $\varepsilon_0, \varepsilon_1$ . On the other hand, using the “correct” value of  $b$  still slightly compensates the drop in dendrite tip velocity with increasing  $\varepsilon_1$ , as demonstrated in Figure 6.

### 5.4. Model comparison

The next set of results illustrates the properties of the  $\Sigma$ P1-P model both with  $b = 1$  and with  $b$  given by (23) in comparison with the original GradP and  $\phi^0$ GradP models.



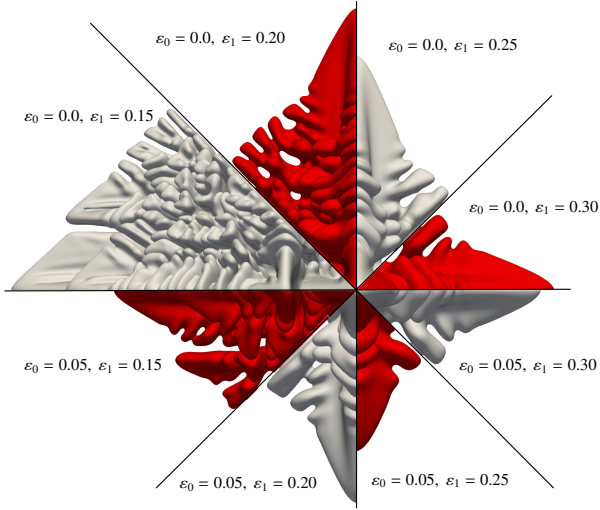


Figure 4: Influence of  $\varepsilon_0, \varepsilon_1$  on the crystal shape obtained by the  $\Sigma P1$ -P model with  $b = 1$ . Details are in Section 5.3.

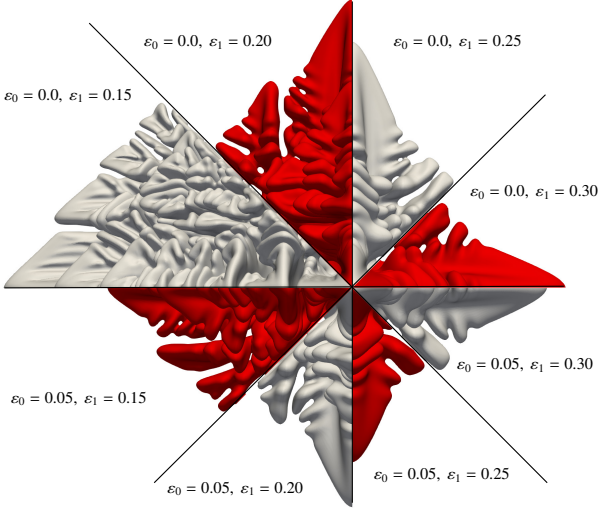


Figure 5: Influence of  $\varepsilon_0, \varepsilon_1$  on the crystal shape obtained by the  $\Sigma P1$ -P model with  $b$  given by (23). Details are in Section 5.3.

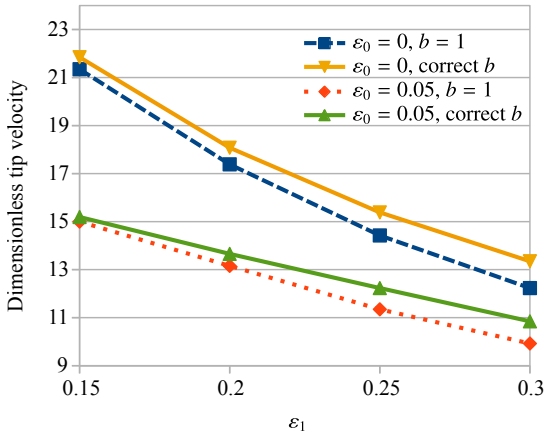


Figure 6: Influence of  $\varepsilon_0, \varepsilon_1$  on the dimensionless dendrite tip velocity in the  $\Sigma P1$ -P model.

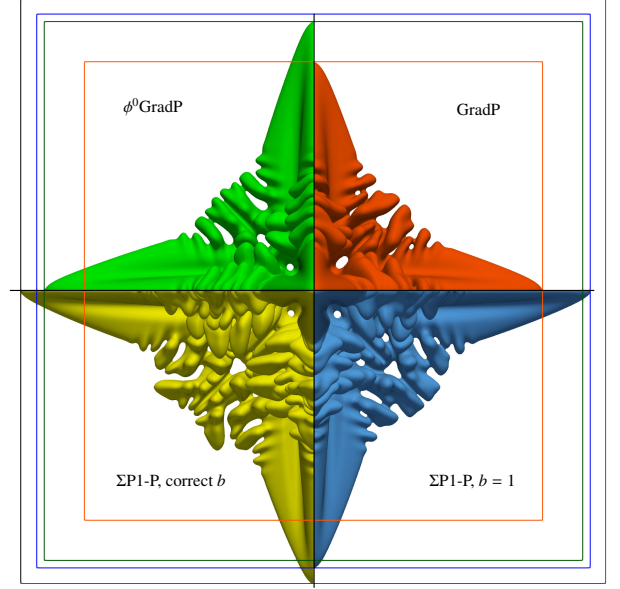


Figure 7: Comparison of crystal shapes obtained by the four reaction term models. The squares indicate the bounding boxes for the individual crystals to assist the visual comparison of average dendrite tip velocities. Details on simulation setup are in Section 5.4.1.

#### 5.4.1. 4-fold anisotropic simulations

Figure 7 demonstrates the solution by all four models at time  $t = 0.32$ . The problem settings are  $\ell = 6$ ,  $N = 600$ , 4-fold anisotropy given by (31) with  $A_1 = 0.02$ , and the nucleation site with radius 0.05 located in the corner of  $\Omega$ . The  $\Sigma P1$ -P model parameters read  $\varepsilon_0 = 0.05$ ,  $\varepsilon_1 = 0.2$ . For this setup, all four models exhibit the same qualitative behavior with slightly different dendrite tip velocities.

In Figure 8, a similar comparison is made at time  $t = 0.4$ , this time with added noise by means of (25) with  $\delta = 0.05$ . The other settings are  $\ell = 8$ ,  $N = 600$ , 4-fold anisotropy with  $A_1 = 0.02$ . Growth symmetries are no longer valid with random thermal fluctuations present. In order to see that, the nucleation site with radius 0.05 is placed in the center of  $\Omega$ . The resulting shapes are indeed asymmetric, but only one octant is visualized for each model in Figure 8. Again, all models are qualitatively commensurate and the noise is shown to induce side branching [43].

Figures 9 and 10 demonstrate the dependence of the solution on the mesh resolution. The parameters for the simulations are the same as in Figure 7 (the first result of this section) except for the changing value of  $N$ . At lower resolutions, the  $\phi^0 \text{GradP}$  model provides more consistent results than the  $\Sigma P1$ -P model. The anisotropic growth is correctly captured by both models from mesh resolution above  $N = 300$  and convergence of the solution in terms of the crystal shape can be observed as  $N$  approaches the finest resolution  $N = 600$ .

Finally, we demonstrate how the  $\phi^0 \text{GradP}$  and  $\Sigma P1$ -P models compare in a simulation with 4-fold anisotropy strength  $A_1 = 0.2$ , which is a value large enough for  $\phi^0$  to lose its convexity property [44]. Such situation is known to yield faceted crystal surfaces [48, 51]. The problem settings are  $\ell = 4$ ,  $N = 200$ ,

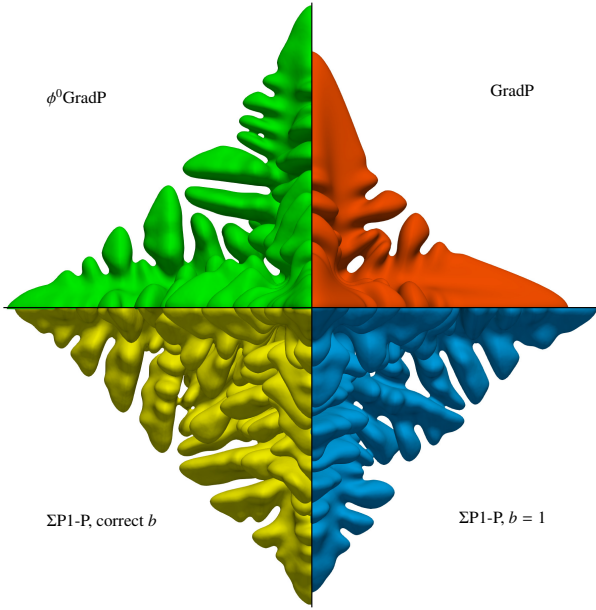


Figure 8: Comparison of crystal shapes obtained by the four reaction term models with random fluctuations of the temperature field. Details on simulation setup are in Section 5.4.1.

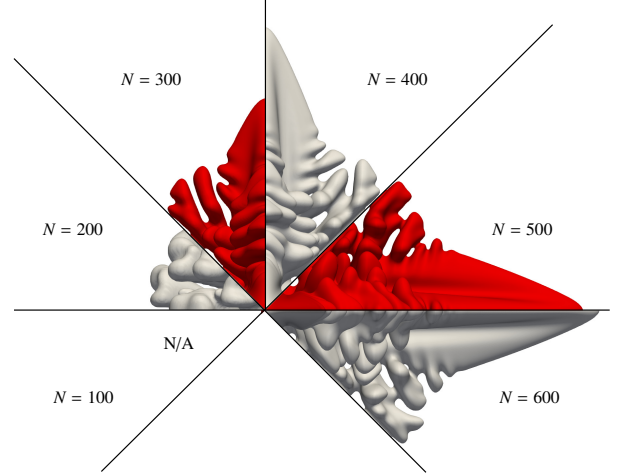


Figure 10: Dependence of the crystal shape on mesh resolution for the  $\Sigma P1-P$  model with  $b = 1$ .

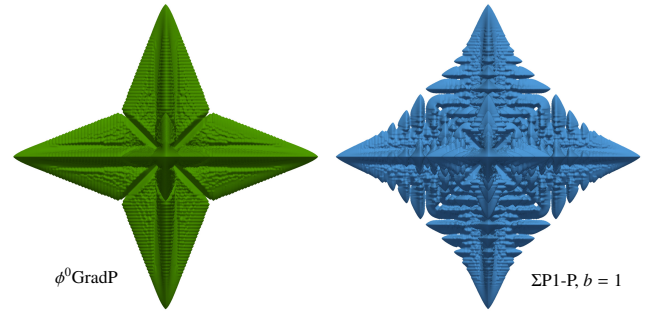


Figure 11: Comparison of crystal shapes produced by the respective models for anisotropy strength beyond the convexity limit for  $\phi^0$ . Both models produce faceted crystal surfaces. Details on simulation setup are in Section 5.4.1.

$t = 0.13$  and the nucleation site is located in the corner of  $\Omega$ . The  $\Sigma P1-P$  model parameters are chosen as  $\varepsilon_0 = 0.05$ ,  $\varepsilon_1 = 0.2$ ,  $b = 1$ . In Figure 11, it is visible that both models produce sharp dendrite tips and facets.

#### 5.4.2. Isotropic Simulations

Figure 12 demonstrates the solution of the simulations of isotropic crystal growth at time  $t = 0.36$ . The settings are the same as in Figure 7 (see Section 5.4.1) except for the anisotropy strength  $A_1 = 0$ , which corresponds to using the isotropic phase field equation (10) instead of (26). In such case, the models GradP and  $\phi^0$ GradP coincide and the  $\Sigma P1-P$  model has the form such that the numerical analysis we performed in [37] applies. Results obtained both without ( $\delta = 0$ ) and with ( $\delta = 0.05$ ) noise given by (25) are provided at the same scale, which testifies to the ability of noise to support crystal growth and branching in a seaweed pattern.

#### 5.5. Physically realistic simulations

Finally, we investigate the behavior of the individual models in the simulation of rapid dendritic solidification of pure nickel. For this situation, a range of both experimental [52, 53, 54] and computational [13, 14] results is available in the literature. The

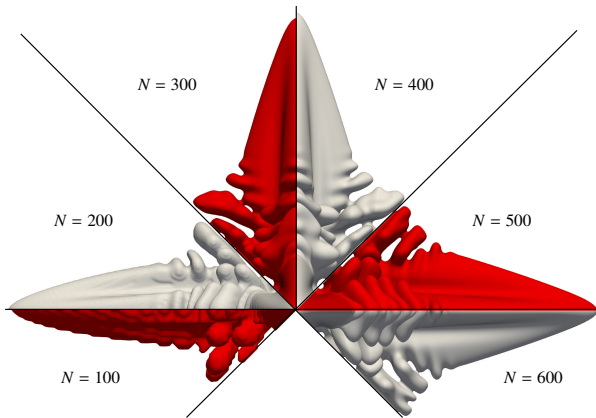


Figure 9: Dependence of the crystal shape on mesh resolution for the  $\phi^0$ GradP model.



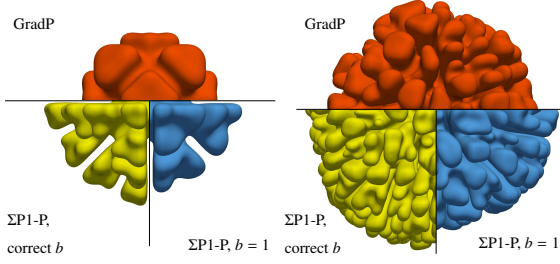


Figure 12: Comparison of crystal shapes obtained by the respective reaction term models in isotropic crystal growth simulations. Results without (left) and with (right) random perturbations of the temperature field. Details on simulation setup are in Section 5.4.2.

Table 3: Physical and computational parameters of rapid solidification of pure Ni under very large supercooling. The relation  $b = 1$  was used for the  $\phi^0$ GradP and  $\Sigma\phi^0$ GradP models and both relations  $b = 1$  and (23) were used for the  $\Sigma$ P1-P model.

Phys. qty	Value	Param.	Value
$\Delta u_{\text{ini}}$	50 – 300 K	$L_0$	10 $\mu\text{m}$
$\rho$	8900 $\text{kg} \cdot \text{m}^{-3}$	$\ell$	2
$c$	609 $\text{J} \cdot \text{kg}^{-1} \cdot \text{K}^{-1}$	$N$	480
$\lambda$	54.2 $\text{W} \cdot \text{m}^{-1} \cdot \text{K}^{-1}$	$\xi$	0.002
$L$	$2.35 \times 10^9 \text{ J} \cdot \text{m}^{-3}$	$\varepsilon_0$	0.05
$u^*$	1728 K	$\varepsilon_1$	0.2
$\sigma$	0.37 $\text{J} \cdot \text{m}^{-2}$	$b$	see caption
$\Delta s$	$1.36 \times 10^6 \text{ J} \cdot \text{m}^{-3} \cdot \text{K}$	$\delta$	0.05
$\mu$	1.99 $\text{m} \cdot \text{s}^{-1} \cdot \text{K}^{-1}$		

models involved in the study are  $\phi^0$ GradP,  $\Sigma\phi^0$ GradP,  $\Sigma$ P1-P without the noise term and  $\Sigma$ P1-P with temperature field perturbation described in Section 3.3. The geometrical setup and initial and boundary conditions are described in Section 5.1. The dimensionless parameters are set using the relations in Table 2 and the physical properties of Ni summarized in Table 3. Table 3 also contains the relevant computational parameters. Again, assuming growth symmetry (see Section 5.1), the nucleation site is located in the corner of  $\Omega$  and its radius in dimensionless coordinates is 0.02. The 2nd order approximation of the anisotropic surface energy for Ni is given by

$$\psi(\mathbf{n}) = 1 + A_1 \left( n_1^4 + n_2^4 + n_3^4 - \frac{3}{5} \right) + A_2 \left[ 3 \left( n_1^4 + n_2^4 + n_3^4 \right) + 66n_1^2 n_2^2 n_3^2 - \frac{17}{7} \right] \quad (32)$$

with  $A_1 = 0.09, A_2 = -0.011$  [14].

Besides observing the crystal morphology, the quantitative evaluation of the simulations consists in calculating the dendrite tip velocity as a function of initial supercooling  $\Delta u_{\text{ini}}$ , which is directly compared with the experimental results obtained in [53] and [52] and the phase-field simulations performed in [13, 14].

#### 5.5.1. Reasons for the choice of computational parameters

A number of computational experiments with the values of  $\Delta u_{\text{ini}}$  in the range given by Table 3 showed that the correct for-

mation of the diffuse but thin phase interface requires the value of  $\xi$  to be small enough, but still several orders of magnitude larger than the interface thickness observed in atomistic simulations [14]. This in turn leads to a minimum requirement on mesh resolution (see Section 2.4). The length scale  $L_0$  and the size of the domain  $\Omega$  given in Table 3 correspond to the domain side length in real coordinates  $\ell L_0 = 20 \mu\text{m}$ . For such settings, the computational costs of the simulations remained feasible: the wall times until the dendrite reached the opposite domain boundary were between 24 and 48 hours on the HELIOS cluster at our department. Each simulation employed three compute nodes equipped with two 16-core AMD EPYC 7281 @2.1GHz CPUs.

Dendrite tip length measurements were performed at solution snapshots corresponding to physical times up to  $2 \mu\text{s}$ . Multiple snapshots were used to ensure that the steady-state dendrite tip velocity was calculated. In comparison, simulations in [13] (also with symmetry taken into account) had a supercooling-dependent domain size up to  $8 \mu\text{m}$  and the experiments in [13], [52] were performed on a time scale of tens of  $\mu\text{s}$ .

The choice of the parameters  $\varepsilon_0, \varepsilon_1$  of the  $\Sigma$ P1-P model was inspired by the findings of Section 5.4.1. In addition, numerical experiments revealed that only some of the combinations investigated earlier in Section 5.3 could be used. For example, with  $\varepsilon_0 = 0$  or  $\varepsilon_1 < 0.15$ , the phase interface did not form correctly and spurious nucleation sites appeared all over the domain  $\Omega$ .

#### 5.5.2. Results

With all four models (see the introduction to Section 5.5 above), simulations for initial supercooling values

$$\Delta u_{\text{ini}} \in \{50 \text{ K}, 80 \text{ K}, 120 \text{ K}, 200 \text{ K}, 300 \text{ K}\}$$

were performed. For  $\Delta u_{\text{ini}} = 50 \text{ K}$ , Figure 13 shows (using parallel projection to the  $xy$  plane) that the crystal morphology is similar for all models. For  $\Delta u_{\text{ini}} = 80 \text{ K}$ , the original  $\phi^0$ GradP model appears to prefer growth along coordinate axes, whereas the remaining model variants produce the longest dendrite in the diagonal direction (which is the expected behavior with anisotropy given by (32) and  $A_1, A_2$  settings given in Section 5.5). Comparing the results of the  $\Sigma$ P1-P with and without noise, it seems like noise promotes the dendrite growth, which was however not confirmed as a general rule by the simulations with deeper supercooling.

With  $\Delta u_{\text{ini}} = 120 \text{ K}$ ,  $\phi^0$ GradP fails after some time, as can be seen in Figure 14. A secondary nucleation site appears spontaneously and another crystal grows from the opposite side of the domain. This is because  $\phi^0$ GradP is not able to maintain the shape of the thin diffuse phase interface and positive values of  $p$  extend far away from the initial position of the interface. The  $\Sigma$ -limited models ( $\Sigma\phi^0$ GradP and  $\Sigma$ P1-P) remain stable and both produce qualitatively similar crystal shapes. Dendrite tip twinning seen with the  $\Sigma\phi^0$ GradP has been observed with the other models too during the numerical experiments and the conditions for its emergence are worth further investigation [55]. As in Section 5.4.1, Figure 14 also shows that noise induces side branching and the transition to a seaweed pattern, which becomes even more pronounced as  $\Delta u_{\text{ini}}$  increases further up to

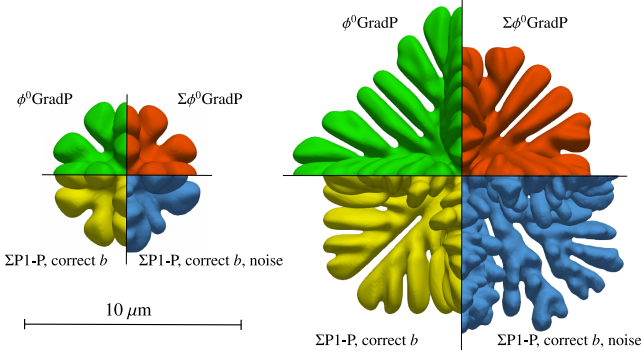


Figure 13: Comparison of crystal shapes obtained by different models for rapid Ni solidification at time  $t = 1.3 \mu\text{s}$  and the initial supercooling  $\Delta u_{\text{ini}} = 50 \text{ K}$  (left) and  $\Delta u_{\text{ini}} = 80 \text{ K}$  (right).

300 K (but this is not demonstrated visually here). In general, our simulations have produced a much more complex and developed dendritic morphology than those in [13].

The dependence of dendrite tip velocity on  $\Delta u_{\text{ini}}$  obtained by simulations with different models together with reference data from literature are plotted in Figures 15 and 16. The original  $\phi^0\text{GradP}$  model failed for  $\Delta u_{\text{ini}} \geq 200$  with spurious nucleation sites spreading all over the computational domain almost immediately after starting the simulation despite  $\Delta u_{\text{ini}}$  being far from the expected onset of homogeneous nucleation [56]. The other models exhibit a reasonable agreement with the reference data. The  $\Sigma\phi^0\text{GradP}$  model gives the highest predictions of dendrite tip velocity slightly above the computations by Bragard et al. [13]. The  $\Sigma\text{P1-P}$  model in all variants yields very similar results that best agree with the measurements by Lum et al. [52], indicating the transition from power-law to linear dependence described both by Lum et al. [52] and Willnecker et al. [53]. The setting of  $b$  has a negligible effect. Adding noise does not generally increase the tip velocity, but it makes the curve more straight (cf. Figure 13 and the related discussion).

## 6. Conclusion

We recalled the asymptotic correspondence [4, 36] between the phase field models used in our previous computational studies [32, 34] and the sharp interface formulation [38]. It is possible to design reaction terms implying different distributions of latent heat release rate across the diffuse interface while keeping the asymptotic properties of the resulting phase field model valid. Inspired by the computationally favorable behavior of the GradP and  $\phi^0\text{GradP}$  models, we proposed an alternative form of the reaction term with a similar latent heat distribution, but completely avoiding the gradient term in (19). The resulting term required further treatment by the  $\Sigma$  limiter (22) to maintain the shape of the thin diffuse interface for larger values of the initial supercooling  $\Delta u_{\text{ini}}$ , which gave rise to the  $\Sigma\text{P1-P}$  model. Unlike the GradP model, the  $\Sigma\text{P1-P}$  model in its isotropic form is compatible with the numerical analysis performed in our related work [37], which provides theoretical justification of the proper function of the implemented finite volume-based numer-

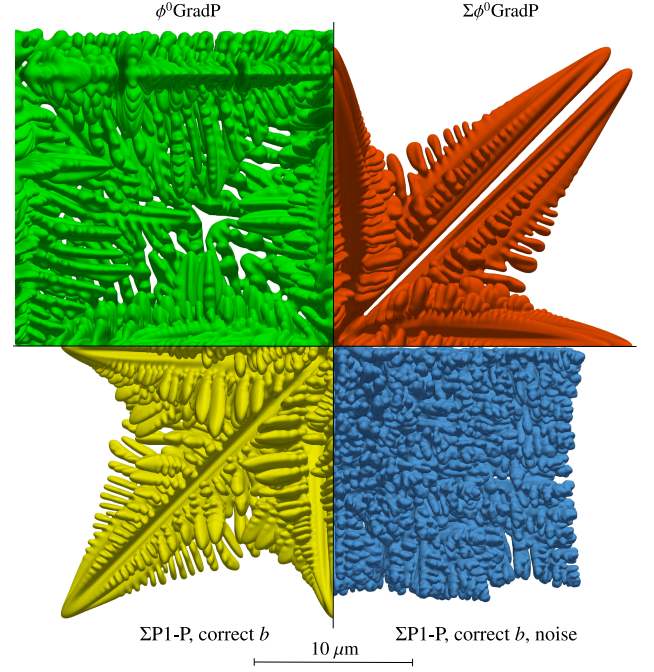


Figure 14: Comparison of crystal shapes obtained by different models for rapid Ni solidification at time  $t = 1.3 \mu\text{s}$  and the initial supercooling  $\Delta u_{\text{ini}} = 120 \text{ K}$ . The  $\phi^0\text{GradP}$  model fails as spurious nucleation sites occur.

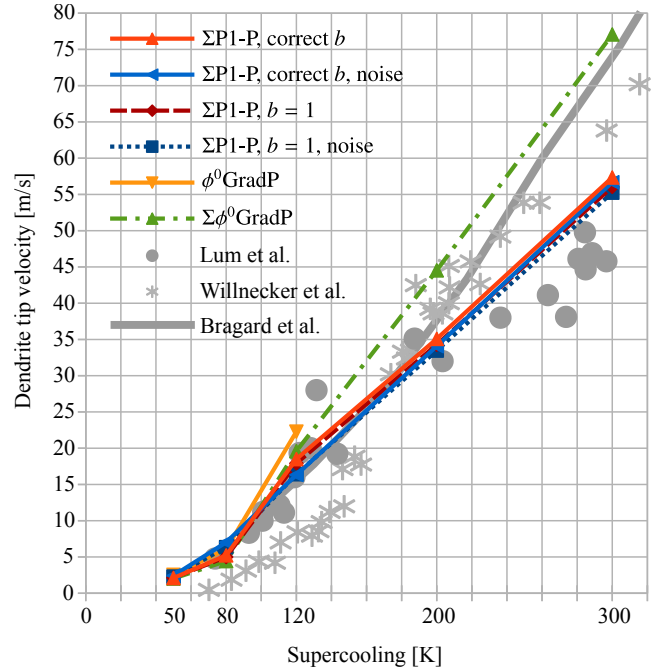


Figure 15: Dendrite tip velocity in pure Ni solidification for large values of supercooling. Results obtained by the different models compared to experimental data by Lum et al. [52] and Willnecker et al. [53] and to phase field simulations by Bragard et al. [13].

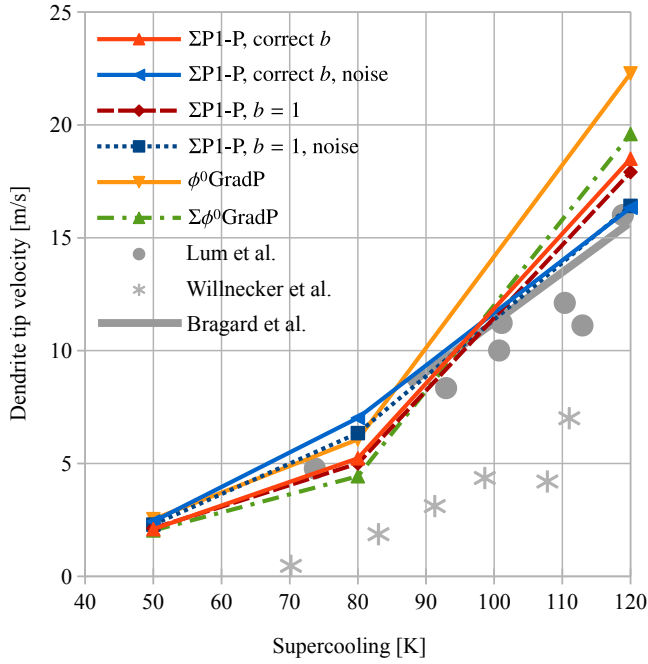


Figure 16: Detail of the plot of dendrite tip velocity in pure Ni solidification for supercooling up to 120 K. Results obtained by the different models compared to experimental data by Lum et al. [52] and Willnecker et al. [53] and to phase field simulations by Bragard et al. [13].

ical solvers. However, the  $\Sigma$  limiter can also be applied to the original GradP and  $\phi^0$ GradP models.

The results of the computations the  $\Sigma$ P1-P model are sensitive to the settings of the  $\Sigma$  limiter parameters  $\varepsilon_0, \varepsilon_1$ . By numerical experiments, we found a setting that produces very similar crystal morphologies to the results of the GradP and  $\phi^0$ GradP models. This setting was also used for successful simulations of rapid solidification of pure nickel that were not possible at all with the GradP and  $\phi^0$ GradP models. However, these promising results deserve additional computational studies. Finer sampling of the initial supercooling range should confirm the model's capability of reproducing the transition from power-law to linear character of the curve in Figure 15, which is observed in the experimental data [53, 52] but not predicted by the earlier phase field simulations [13]. Simulations with varying anisotropy strength parameters  $A_1, A_2$  should reveal the behavior of the proposed model with respect to the resulting crystal morphology, which can be compared e.g. with the recent results in [55].

#### Data availability

The datasets and computer codes are available upon request from the authors.

#### Declaration of Competing Interest

The authors declare that they have no known competing financial interests or personal relationships that could have appeared to influence the work reported in this paper.

#### CRediT authorship contribution statement

**Pavel Strachota:** Conceptualization, Methodology, Software, Validation, Formal analysis, Investigation, Data Curation, Writing - Original Draft, Writing - Review & Editing, Visualization. **Aleš Wodecki:** Methodology, Writing - Review & Editing. **Michal Beneš:** Writing - Review & Editing, Supervision, Project administration.

#### Acknowledgments

This work is part of the project *Centre of Advanced Applied Sciences* (Reg. No. CZ.02.1.01/0.0/0.0/16-019/0000778), co-financed by the European Union. Partial support of grant No. SGS20/184/OHK4/3T/14 of the Grant Agency of the Czech Technical University in Prague.

#### References

- [1] N. Provatas, K. Elder, *Phase-Field Methods in Materials Science and Engineering*, WILEY-VCH Verlag, 2010.
- [2] W. J. Boettinger, S. Coriell, A. L. Greer, A. Karma, W. Kurz, M. Rappaz, R. Trivedi, Solidification microstructures: Recent developments, future directions, *Acta Mater.* 48 (2000) 43–70.
- [3] S. Allen, J. W. Cahn, A microscopic theory for antiphase boundary motion and its application to antiphase domain coarsening, *Acta Metall.* 27 (1979) 1084–1095.
- [4] G. Caginalp, Stefan and Hele-Shaw type models as asymptotic limits of the phase-field equation, *Phys. Rev. A* 39 (1989) 5887–5896.
- [5] G. Caginalp, X. Chen, Convergence of the phase field model to its sharp interface limits, *Eur. J. Appl. Math.* 9 (1998) 417–445.
- [6] A. A. Wheeler, B. T. Murray, R. J. Schaefer, Computation of dendrites using a phase field model, *Physica D* 66 (1993) 243–262.
- [7] R. Kobayashi, Modeling and numerical simulations of dendritic crystal growth, *Physica D* 63 (1993) 410–423.
- [8] R. Kupferman, O. Shochet, E. Ben-Jacob, Numerical study of a morphology diagram in the large undercooling limit using a phase-field model, *Phys. Rev. E* 50 (1993) 1005–1008.
- [9] C. M. Elliott, A. R. Gardiner, *Double Obstacle Phase Field Computations of Dendritic Growth*, Technical Report 96/19, University of Sussex at Brighton, 1996.
- [10] A. A. Wheeler, W. J. Boettinger, G. B. McFadden, Phase-field model for isothermal phase transitions in binary alloys, *Phys. Rev. A* 45 (1992) 7424–7440.
- [11] A. Karma, W.-J. Rappel, Numerical simulation of three-dimensional dendritic growth, *Phys. Rev. Lett.* 77 (1996) 4050–4053.
- [12] A. Karma, W.-J. Rappel, Quantitative phase-field modeling of dendritic growth in two and three dimensions, *Phys. Rev. E* 57 (1998) 4.
- [13] J. Bragard, A. Karma, Y. H. Lee, Linking phase-field and atomistic simulations to model dendritic solidification in highly undercooled melts, *Interface Sci.* 10 (2002) 121–136.
- [14] J. Hoyt, M. Asta, A. Karma, Atomistic and continuum modeling of dendritic solidification, *Mater. Sci. Eng. R* 41 (2003) 121–163.
- [15] J. C. Ramirez, C. Beckermann, A. Karma, H.-J. Diepers, Phase-field modeling of binary alloy solidification with coupled heat and solute diffusion, *Phys. Rev. E* 69 (2004) 051607.
- [16] B. Nestler, H. Garcke, B. Stinner, Multicomponent alloy solidification: Phase-field modeling and simulations, *Phys. Rev. E* 71 (2005) 041609.
- [17] J.-H. Jeong, N. Goldenfeld, J. A. Dantzig, Phase field model for three-dimensional dendritic growth with fluid flow, *Phys. Rev. E* 64 (2001) 041602.
- [18] Y. Suwa, Y. Saito, Computer simulation of grain growth by the phase field model. Effect of interfacial energy on kinetics of grain growth, *Mater. Trans.* 44 (2003) 2245–2251.
- [19] Y. Suwa, *Phase-field Simulation of Grain Growth*, Technical Report 102, Nippon Steel, 2013.

- [20] H.-K. Kim, S. G. Kim, W. Dong, I. Steinbach, B.-J. Lee, Phase-field modeling for 3D grain growth based on a grain boundary energy database, *Modelling Simul. Mater. Sci. Eng.* 22 (2014) 034004.
- [21] T. Takaki, M. Ohno, Y. Shibuta, S. Sakane, T. Shimokawabe, T. Aoki, Two-dimensional phase-field study of competitive grain growth during directional solidification of polycrystalline binary alloy, *J. Cryst. Growth* 442 (2016) 14–24.
- [22] R. Rojas, T. Takaki, M. Ohno, A phase-field-lattice boltzmann method for modeling motion and growth of a dendrite for binary alloy solidification in the presence of melt convection, *J. Comput. Phys.* 298 (2015) 29–40.
- [23] T. Takaki, R. Rojas, M. Ohno, T. Shimokawabe, T. Aoki, GPU phase-field lattice Boltzmann simulations of growth and motion of a binary alloy dendrite, *IOP Conf. Ser.: Mater. Sci. Eng.* 84 (2015) 012066.
- [24] Y. Shibuta, M. Ohno, T. Takaki, Solidification in a supercomputer: From crystal nuclei to dendrite assemblages, *JOM* 67 (2015) 1793–1804.
- [25] Q. Du, M. Li, C. Liu, Analysis of a phase field Navier-Stokes vesicle-fluid interaction model, *Discrete. Cont. Dyn. S. B* 8 (2007) 539–556.
- [26] C. Miehe, L.-M. Schänzel, H. Ulmer, Phase field modeling of fracture in multi-physics problems. part I. balance of crack surface and failure criteria for brittle crack propagation in thermo-elastic solids, *Comput. Method. Appl. M.* 294 (2015) 449–485.
- [27] S. Kurima, Asymptotic analysis for Cahn-Hilliard type phase-field systems related to tumor growth in general domains, *Math. Methods Appl. Sci.* 42 (2019) 2431–2454.
- [28] J. Kim, A generalized continuous surface tension force formulation for phase-field models for multi-component immiscible fluid flows, *Comput. Methods Appl. Mech. Engrg.* 198 (2009) 3105–3112.
- [29] M. Beneš, Mathematical and computational aspects of solidification of pure substances, *Acta Math. Univ. Comenianae* 70 (2001) 123–151.
- [30] M. Beneš, Computational studies of anisotropic diffuse interface model of microstructure formation in solidification, *Acta Math. Univ. Comenianae* 76 (2007) 39–59.
- [31] M. Beneš, D. Hilhorst, R. Weidenfeld, Interface dynamics for an anisotropic Allen-Cahn equation, *Nonlocal Elliptic and Parabolic Problems* 66 (2004) 39–45.
- [32] P. Strachota, M. Beneš, Design and verification of the MPFA scheme for three-dimensional phase field model of dendritic crystal growth, in: A. Cangiani, R. L. Davidchack, E. Georgoulis, A. N. Ghorban, J. Levesley, M. V. Tretyakov (Eds.), *Numerical Mathematics and Advanced Applications 2011: Proceedings of ENUMATH 2011, the 9th European Conference on Numerical Mathematics and Advanced Applications*, Leicester, September 2011, Springer Berlin Heidelberg, 2013, pp. 459–467.
- [33] P. Strachota, M. Beneš, A hybrid parallel numerical algorithm for three-dimensional phase field modeling of crystal growth, in: A. Handlovičová, D. Ševčovič (Eds.), *ALGORITMY 2016, 20th Conference on Scientific Computing, Vysoké Tatry - Podbanské, Slovakia, March 14 - 18, 2016. Proceedings of contributed papers and posters*, Comenius University, Bratislava, 2016, pp. 23–32.
- [34] P. Strachota, A. Wodecki, High resolution 3D phase field simulations of single crystal and polycrystalline solidification, *Acta Phys. Pol. A* 134 (2018) 653–657.
- [35] P. Strachota, A. Wodecki, M. Beneš, Efficiency of a hybrid parallel algorithm for phase-field simulation of polycrystalline solidification in 3D, in: P. Frolkovič, K. Mikula, D. Ševčovič (Eds.), *ALGORITMY 2020, 21th Conference on Scientific Computing, Vysoké Tatry - Podbanské, Slovakia, September 10 - 15, 2020. Proceedings of contributed papers and posters*, SPEKTRUM STU, 2020, pp. 131–140.
- [36] M. Beneš, Mathematical analysis of phase-field equations with numerically efficient coupling terms, *Interface. Free. Bound.* 3 (2001) 201–221.
- [37] A. Wodecki, P. Strachota, M. Beneš, Convergence of the finite volume method on unstructured meshes for a 3D phase field model of solidification, *arXiv (arXiv:2010.04132)* (2020) 1–21.
- [38] M. E. Gurtin, On the two-phase Stefan problem with interfacial energy and entropy, *Arch. Ration. Mech. An.* 96 (1986) 199–241.
- [39] P. Strachota, Analysis and Application of Numerical Methods for Solving Nonlinear Reaction-Diffusion Equations, Ph.D. thesis, Czech Technical University in Prague, 2012.
- [40] M. Beneš, Diffuse-interface treatment of the anisotropic mean-curvature flow, *Appl. Math-Czech.* 48 (2003) 437–453.
- [41] M. Beneš, Anisotropic phase-field model with focused latent-heat release, in: *FREE BOUNDARY PROBLEMS: Theory and Applications II*, volume 14 of *GAKUTO International Series in Mathematical Sciences and Applications*, pp. 18–30.
- [42] M. Beneš, P. Strachota, Z. Čulík, Quantitative aspects of microstructure formation in solidification, in: El-Azab (Ed.), *Multiscale Materials Modeling 2008*, Florida State University, 2008, pp. 746–751.
- [43] A. Karma, W.-J. Rappel, Phase-field model of dendritic sidebranching with thermal noise, *Phys. Rev. E* 60 (1999) 3614–3625.
- [44] G. Bellettini, M. Paolini, Anisotropic motion by mean curvature in the context of Finsler geometry, *Hokkaido Math. J.* 25 (1996) 537–566.
- [45] P. Strachota, Antidissipative numerical schemes for the anisotropic diffusion operator in problems for the Allen-Cahn equation, in: A. Handlovičová, P. Frolkovič, K. Mikula, D. Ševčovič (Eds.), *ALGORITMY 2009 - Proceedings of contributed lectures and posters*, volume 18, Slovak University of Technology in Bratislava, 2009, pp. 134–142.
- [46] P. Strachota, M. Beneš, A multipoint flux approximation finite volume scheme for solving anisotropic reaction-diffusion systems in 3D, in: J. Fořt, J. Fürst, J. Halama, R. Herbin, F. Hubert (Eds.), *Finite Volumes for Complex Applications VI - Problems & Perspectives*, Springer, 2011, pp. 741–749.
- [47] R. E. Napolitano, S. Liu, Three-dimensional crystal-melt Wulff-shape and interfacial stiffness in the Al-Sn binary system, *Phys. Rev. B* 70 (2004) 214103.
- [48] M. E. Gurtin, *Thermomechanics of Evolving Phase Boundaries in the Plane*, Oxford Mathematical Monographs, Oxford University Press, 1993.
- [49] M. PunKay, Modeling of anisotropic surface energies for quantum dot formation and morphological evolution, in: *NNIN REU Research Accomplishments*, University of Michigan, 2005, pp. 116–117.
- [50] J. Christiansen, Numerical solution of ordinary simultaneous differential equations of the 1st order using a method for automatic step change, *Numer. Math.* 14 (1970) 317–324.
- [51] R. Kobayashi, Y. Giga, On anisotropy and curvature effects for growing crystals, *Japan J. Indust. Appl. Math.* 18 (2001) 207–230. Recent topics in mathematics moving toward science and engineering.
- [52] J. W. Lum, D. M. Matson, M. C. Flemings, High-speed imaging and analysis of the solidification of undercooled nickel melts, *Metall. Mater. Trans. B* 27B (1996) 865–870.
- [53] R. Willnecker, D. M. Herlach, B. Feuerbacher, Evidence of nonequilibrium processes in rapid solidification of undercooled metals, *Phys. Rev. Lett.* 62 (1989) 2707–2710.
- [54] D. M. Herlach, Non-equilibrium solidification of undercooled metallic melts, *Metals* 4 (2014) 196–234.
- [55] G. Kim, T. Takaki, Y. Shibuta, S. Sakane, M. O. Kiyotaka Matsuura, A parametric study of morphology selection in equiaxed dendritic solidification, *Comput. Mater. Sci.* 162 (2019) 76–81.
- [56] A. Filippini, A. D. Cicco, S. D. Panfilis, P. Giammatteo, F. Iesari, Crystalline nucleation in undercooled liquid nickel, *Acta Mater.* 124 (2017) 261–267.